Surface Structure Analysis and Atomic Force Microscopy Simulation Using DFT

Masahiro FUKUDA
Institute for Solid State Physics, University of Tokyo
Kashiwa-no-ha, Kashiwa, Chiba 277-8581

Abstract

We review recent studies on the structure analysis of silicene on Ag(111) and diamond (001) surfaces using atomic force microscopy (AFM), its simulations based on density functional theory (DFT), and regional chemical potential (RCP) analysis. These studies are expected to contribute to atomic-scale material design and to the understanding of surface structures and their formation processes.

1 Introduction

In recent years, advances in experimental techniques such as Scanning Tunneling Microscopy (STM) and AFM have expanded the scope of condensed matter physics from bulk properties of solids to surface properties of materials. At material surfaces, phenomena such as crystal growth and surface reactions occur that cannot be explained solely by bulk properties, making this a highly attractive field of research. On the other hand, in the field of theoretical calculations, advancements such as band structure analysis using the unfolding method [1] and the development of computational methods for calculating absolute core-level binding energies in solids [2] have made it possible to directly compare experimental results with electronic structure calculations based on DFT. As a result, DFT calculations are playing an increasingly important role in understanding surface states of solids.

Furthermore, large-scale electronic structure calculations now allow for the direct evaluation of electron transmission probabilities and interatomic forces between a probe and a material surface, enabling detailed comparisons with STM and AFM measurements. In other words, improvements in computational performance, the development of computational methods, and the advancement of massively parallel first-principles calculation codes have created an environment where large-scale first-principles calculations on realistic systems are feasible, paving the way for close collaboration between theory and experiment.

In this report, we present our recent studies on the identification of surface structures and the evaluation of interactions with AFM tips [3–5], conducted through a combination of AFM experiments and DFT calculations by OpenMX [6]. Particular emphasis is placed on the computational aspects, with a detailed discussion of the DFT calculation process for material surfaces and force calculations for AFM simulation. Furthermore, we report the proposal of a novel analysis and visualization method based on the RCP, which enables the prediction of chemical bonding forces between material surfaces and AFM tip [7].

2 DFT calculations for material surfaces

In this section, we describe how to construct surface structures by DFT calculations, using recent our study of 4×4 silicene on an

Ag(111) surface [3] as a representative example. The computational details are described in Appendix A.

First, we performed geometry optimization and cell optimization of the bulk Ag structure using its primitive cell. The obtained primitive cell was symmetrized using spglib [8], because slight distortions in the primitive cell can affect the behavior of band degeneracy points when applying band structure calculations such as the unfolding method for surface structures.

Next, we constructed a layered slab structure with a (111) surface orientation based on the optimized primitive cell. The thickness of the atomic layers was set to approximately 5–7 layers. In systems where a two-dimensional material such as silicene is adsorbed on the substrate surface, particular care must be taken, since the structure of the 2D material can be significantly influenced by the slab thickness.

In some cases, even increasing the slab thickness may not be sufficient to prevent the electronic states from the dangling bonds on the bottom side of the substrate from affecting the surface electronic structure. In such cases, surface passivation, such as hydrogen termination, may be required.

Subsequently, we performed geometry optimization for the primitive cell of Ag(111) surface, with the bottom two atomic layers fixed. A vacuum layer of about 20 Å was inserted along the surface normal direction to eliminate periodic interactions in that direction. In OpenMX, the number of grids which is determined by the cell size and the energy cutoff is used both for numerical integrations and for solving the Poisson equation. Therefore, careful attention must be paid to these parameters.

Finally, we constructed a supercell of the Ag(111) surface and placed a silicene structure on top, followed by geometry optimization.

3 Identification of the structures of silicene on Ag(111) surface

It is difficult to theoretically predict how silicene buckles and forms a commensurate structure with the Ag(111) surface, due to the vast number of possible initial configurations. Therefore, experimental insight into the structure model is essential for guiding theoretical calculations. In Ref. [3], the AFM topography image shown in a pink lattice of Fig. 1 (a) suggested that 4×4 α-phase silicene (Fig. 2 (a)) is observed on the Ag(111) surface.

In addition, a structure with a Si adatom on silicene was also observed as shown in a black lattice of Fig. 1 (a) and (b), and it was suggested that this corresponds to the 4×4 β-T4′-phase (Fig. 2 (d)). However, in the AFM experiment, the atomic structure of the underlying silicene cannot be clearly identified due to the influence of the Si adatom located at the top. To determine the stable silicene structure with a Si adatom, DFT calculations were performed under various computational conditions as shown in Table 1 using the 4×4 α-phase and 4×4 β-phase as initial guesses. Based on the DFT results with a $3 \times 3 \times 1$ k-point mesh, an energy cutoff of 300 Ry, and a 7-layer Ag slab model, it was revealed that the α-phase silicene transitions to the β-T4′-phase as a result of the addition of a Si adatom. In this study, we have paved the way for material design by inducing a phase transition in silicene through the manipulation of silicon adatoms using an AFM probe.

4 Force curve and topography of AFM

Since AFM estimates the positions and heights of atoms based on the magnitude of interatomic forces, it does not necessarily determine the exact nuclear positions of the most stable structure. Therefore, in some cases, it can be

Table 1: Relative energy convergence for the number of Ag layers by GGA with a $3 \times 3 \times 1$ ($1 \times 1 \times 1$) mesh of k points and the cut off energy $E_{cut} = 300$(Ry) (220(Ry)). The values in red represent more stable phase. Adapted from Ref. [3], Copyright (2023), with permission from Elsevier.

Accuracy	Phase	Adatom	Relative energy (eV)				
			3 layers	5 layers	6 layers	7 layers	8 layers
k-point: $1 \times 1 \times 1$,	α	no	0.0000	0.2147	0.2398	—	—
$E_{cut} = 220$(Ry)	β	no	0.0953	0.0000	0.0000	—	—
	α	no	0.0000	0.0179	0.0000	0.0000	0.0000
k-point: $3 \times 3 \times 1$,	β	no	0.0997	0.0000	0.0087	0.0645	0.0490
$E_{cut} = 300$(Ry)	α	T4'	0.0036	0.0061	0.4489	0.4398	0.4025
	β	T4'	0.0000	0.0000	0.0000	0.0000	0.0000

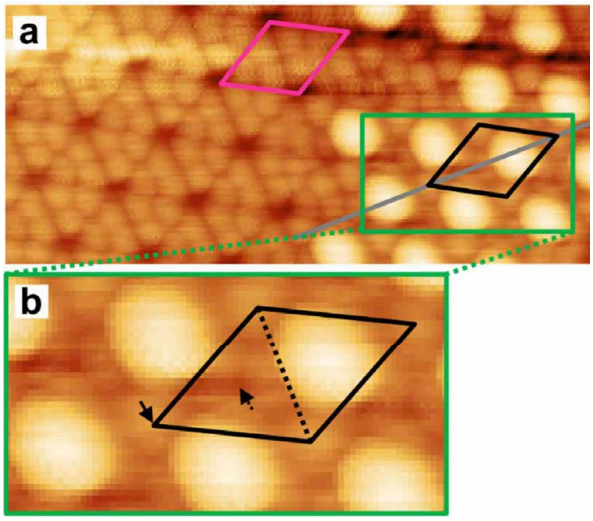

Figure 1: AFM topographic images of 4×4 silicene on Ag(111) surface. The lattice in pink (black) represents primitive cell of α-phase (β-T4′-phase). Adapted from Ref. [3], Copyright (2023), with permission from Elsevier.

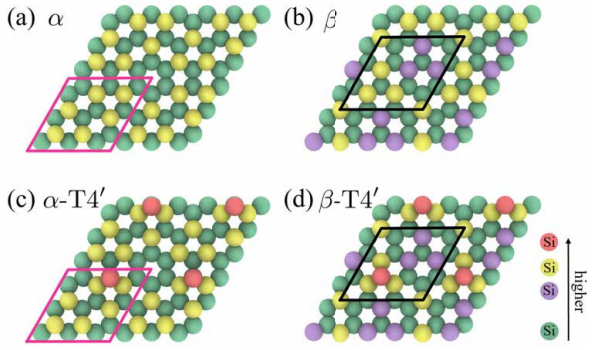

Figure 2: (a) α-phase, (b) β-phase, (c) α-T4′-phase, and (d) β-T4′-phase of 4×4 silicene on Ag(111) surface. Adapted from Ref. [3], Copyright (2023), with permission from Elsevier.

crucial to compute the interatomic forces between the AFM tip model and the surface using DFT calculations for comparison with experimental results.

As models for non-contact or near-contact AFM tips, structures formed on Si(111) (Fig. 3(a)) and Si(001) surfaces (Fig. 3(b)) are commonly used [9–11]. These tips have a dangling bond protruding from the apex atom, which can generate a strong attractive force due to chemical bonding when the surface atoms are chemically active. This strong interaction enables high-resolution AFM topographic imaging.

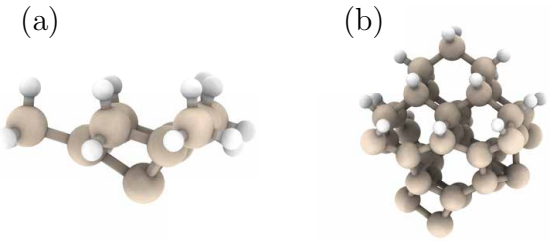

Figure 3: Models of Si tip formed on (a) Si(111) surface and (b) Si(001) surface. The spheres in white represent hydrogen terminations. The other spheres represent Si atoms.

It is known that the tip formed on Si(111) surface tends to exhibit stronger chemical bonding interactions with the material surface. While both models often reproduce experimentally observed interatomic forces well, they should be used carefully. This is because in cases with highly corrugated surface structures, atoms other than the apex atom may in-

Total force acting on nuclei

$$F = \sum_{k=1}^{N_{\mathrm{atom}}} \frac{\partial E_{tot}}{\partial \tau_k} \qquad \tau_k : \text{coordinates for nuclei}$$

$$= \sum_{k=1}^{N_{\mathrm{tip}}} \frac{\partial E_{tot}}{\partial \tau_k^t} + \sum_{k=1}^{N_{\mathrm{sample}}} \frac{\partial E_{tot}}{\partial \tau_k^s}$$

Force between the tip and the surface

$$F_{ts} = \sum_{k=1}^{N_{\mathrm{tip}}} \frac{\partial E_{tot}}{\partial \tau_k^t}$$

$$\Delta E_{tot}(z) \approx \sum_{k=1}^{N_{\mathrm{tip}}} \frac{\partial E_{tot}(z)}{\partial \tau_k^t} \Delta z$$

$$\therefore F_{ts}(z) = \frac{dE_{tot}(z)}{dz} \approx \sum_{k=1}^{N_{\mathrm{tip}}} \frac{\partial E_{tot}(z)}{\partial \tau_k^t}$$

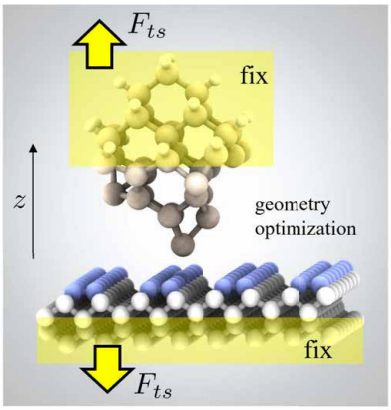

Figure 4: DFT force calculation method for AFM.

teract with the surface. In experiments, chemically inactive tips are also sometimes employed by attaching a CO molecule to the apex of the AFM tip.

The force calculation method based on DFT is summarized in Fig. 4. The structure was optimized while fixing the uppermost atoms of the tip and the bottom atoms of the substrate. The interatomic force acting on the tip was calculated as the sum of the Hellmann–Feynman forces acting on the atoms composing the tip.

In our study of the atomic observation on diamond (001) dimer surfaces with/without hydrogen termination [4], we experimentally demonstrated that strong chemical bonding between C–C dimers on the surface and the AFM tip leads to high-resolution AFM topographic imaging as shown in Fig. 5. In addition, it was found that the distance between the local minima in the force, which arises from the interaction with the AFM tip rather than the original interatomic distance, agrees well between the experimental observations and the DFT calculations using an AFM tip model (Fig. 3 (a)). This revealed that partial breaking of the dimer bonds occurs during the interaction as shown in Fig. 5.

Another example of a force curve obtained from DFT calculations was presented in Ref. [5], where a five-carbon-dimer ribbon on a clean diamond (001) surface was investigated, as shown in Fig. 6. According to the constant-force AFM results shown in Figs. 6 (a) and (c), the tip height becomes lower over the atoms of the dimers at both ends of the dimer ribbon, giving the impression that the edge dimers are located at a lower height. However, geometry optimization using DFT showed no significant difference in atomic height. To investigate this, we calculated force curves during constant-height lateral movement across the same path as the experiment and found that the force acting on the edge dimer atoms was indeed weaker. What, then, causes the weaker force observed on the edge dimer atoms? This will be clarified in the following section based on an analysis using the RCP. Although we do not discuss it in detail here, in our study of Ref. [5], formation energies were calculated by DFT for various dimer ribbons on the clean diamond (001) surface. The results indicate that ribbons composed of an odd number of dimers are more stable, which was confirmed by high-resolution AFM observations. This may provide a guideline for future structural predictions and insights into growth mechanisms of diamond surfaces.

5 Visualization of chemical active region

As discussed above, the atomic positions obtained from geometry optimization by DFT are not sufficient to fully interpret AFM im-

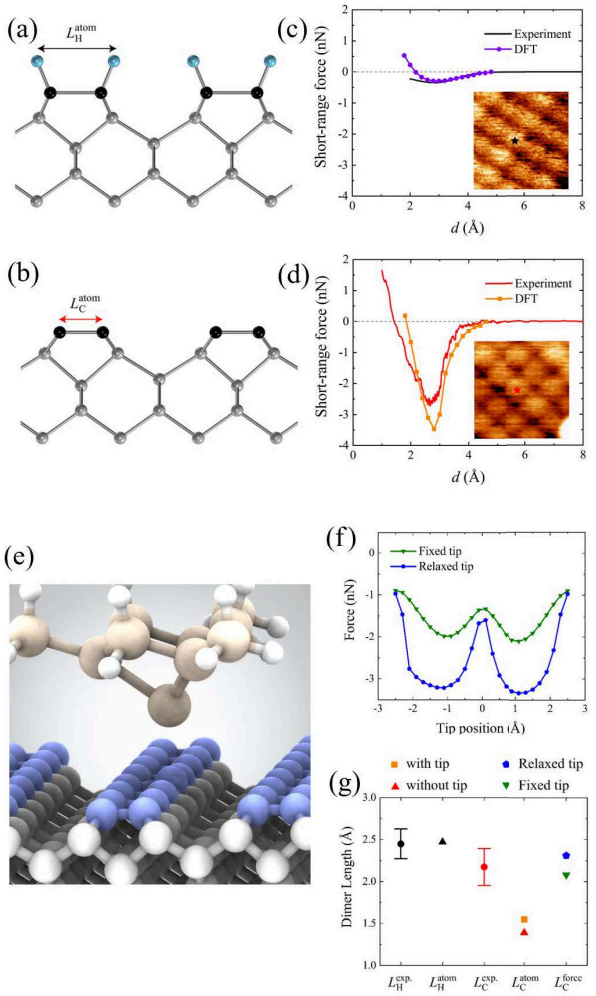

Figure 5: Side views of (a) a model of hydrogenated diamond (001) and (b) a model of clean diamond (001). Force curves for (c) hydrogenated diamond (001) and (d) clean diamond (001) with the tip during vertical movement. (e) One of the models for DFT force curve calculations. The sphere in blue represent the C-C dimer formed on the diamond (001) surface. (f) Force acting on the tip during lateral movement across the C–C dimer bond, with and without atomic relaxation of the tip. (g) Dimer length obtained by AFM experiment and DFT calculations. Distance between the local minima in force (L_C^{force}) for a fixed/relaxed tip was estimated from Fig.(f). Adapted from Ref. [4], Copyright (2025), American Chemical Society.

ages. This is because chemically active regions, such as dangling bonds and double bonds on the material surface, can strongly interact with the dangling bond of the Si tip in the AFM, resulting in behavior that differs significantly from other regions. Recent our theoretical study revealed that a local RCP analysis method based on an energy window scheme [7] enables us to quantitatively estimate the selectivity of atomic and molecular adsorption on surfaces, as well as the strength of chemical bonding forces between a probe tip and a surface in AFM measurements.

The local RCP is defined as

$$\mu_R^\tau(\vec{r}) \equiv \frac{\Delta\varepsilon_\tau(\vec{r})}{\Delta n(\vec{r})} \approx \frac{\varepsilon_{\tau,\mathrm{ew}}(\vec{r})}{n_{\mathrm{ew}}(\vec{r})}, \tag{1}$$

where $\Delta\varepsilon_\tau(\vec{r})$ and $\Delta n(\vec{r})$ are variations of regional energy density and electron number density, respectively, under a given perturbative electron excitation. We call the last approximation an "energy window scheme", where the physical quantities are calculated in an energy range of $\mu_{\mathrm{low}} < \mu < \mu_{\mathrm{up}}$ using the Fermi function with broadening factors $\tilde{T}_{\mathrm{low}}$ and $\tilde{T}_{\mathrm{up}}$ as follows.

$$n_{\mathrm{ew}}(\vec{r}) = \int_{-\infty}^{\infty} dE n(\vec{r},E)\left[f_{\mathrm{up}}(E) - f_{\mathrm{low}}(E)\right], \tag{2}$$

$$\varepsilon_{\tau,\mathrm{ew}}(\vec{r}) = \int_{-\infty}^{\infty} dE \varepsilon_\tau(\vec{r},E)\left[f_{\mathrm{up}}(E) - f_{\mathrm{low}}(E)\right], \tag{3}$$

where the Fermi function is defined as $f_\lambda(E) \equiv f(E,\mu_\lambda,\tilde{T}_\lambda) \equiv 1/(1+e^{(E-\mu_\lambda)/\tilde{T}_\lambda})$. The energy-dependent electron number density $n(\vec{r},E)$ and regional energy density $\varepsilon_\tau(\vec{r},E)$ are given in Appendix in Ref. [7]. The local RCP, in contrast to the conventional chemical potential, is spatially dependent, and the value of the local RCP on the material surface $\mu_R^\tau(\vec{r}_{\mathrm{surf}})$ indicates the chemical activity originating from the electron-donating ability at each point.

We have developed a highly parallelized local physical quantity calcula-

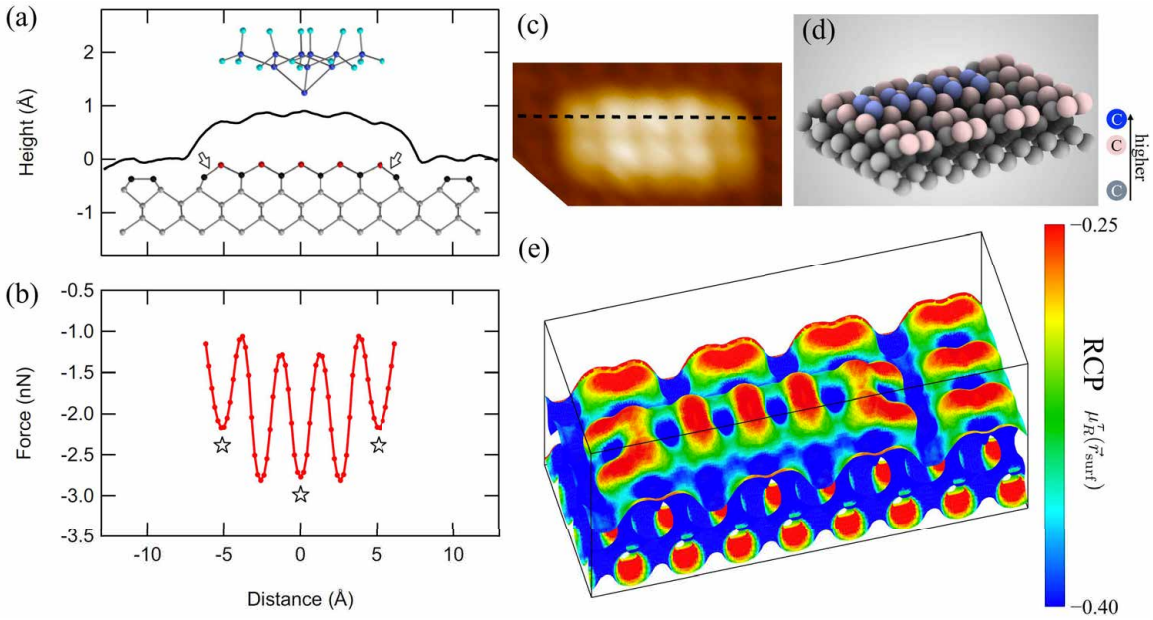

Figure 6: (a) Line profile of a five carbon dimers ribbon on the black dotted line of the AFM topographic image shown in (c), and (b) corresponding force acting on the tip during a constant height scan 3Å above the carbon atoms of the dimer ribbon before relaxation along one side of the ribbon, indicated by the black dotted line in (c). (d) Structure model of the five carbon dimers ribbon on the clean diamond (001) surface. (e) Regional chemical potential $\mu_R^\tau(\vec{r}_{\rm surf})$ in the energy range between -2 eV and 0 eV plotted on the material surface defined by zero kinetic energy density. Adapted from Ref. [5], licensed under CC BY 4.0, and Ref. [7].

tion code, FLPQ [12], which supports MPI/OpenMP hybrid parallel calculations, and FLPQViewer [13] to visualize the local RCP. In Fig. 6 (e), the distribution of the local RCP on the surface, which is defined by the zero kinetic energy density, for five carbon dimers ribbon on the diamond (001) surface is visualized. The red region shown in Fig. 6 (e) corresponds to the high local RCP originating from the C-C double bonds, which are highly chemically active regions. The Fig. 6 (e) revealed that the dimers previously thought to be located at both ends actually form double bonds with the underlying carbon atoms, indicating that their electronic states are essentially different from those of the central dimers. This RCP analysis has paved the way for understanding the chemically active regions on the material surface at the atomic scale.

6 Summary

In this report, we have reviewed our recent studies [3–5, 7] on surface structure analysis and AFM simulation using DFT, focusing on computational aspects. The combined approach of numerical simulations and experimental investigations is expected to shed light on unexplored atomic-scale surface structures and their formation processes.

7 Acknowledgement

I would like to thank Taisuke Ozaki, Yoshiaki Sugimoto, Masato Senami, Yuuki Yasui, Yuuki Adachi, Runnan Zhang, Masahiko Ogura, Toshiharu Makino, and Daisuke Takeuchi for their valuable support and collaboration on various aspects of these research. The computation in these work has been done using the facilities of the Supercomputer Center, the Institute for Solid State Physics, the University

of Tokyo (ISSPkyodo-SC-2023-Ba-0073, 2024-Ba-0053).

A Computational details

The DFT calculations within a generalized gradient approximation (GGA) [14, 15] were performed for the geometry relaxations and variable cell optimizations using the OpenMX code [6] based on norm-conserving pseudopotentials generated with multireference energies [16] and optimized pseudoatomic basis functions [17]. The standard basis set we used are listed in OpenMX website [18]. The qualities of the basis functions and fully relativistic pseudopotentials were carefully benchmarked by the delta gauge method [19] to ensure the accuracy of our calculations. An electronic temperature of 300 K is used to count the number of electrons by the Fermi-Dirac function. The regular mesh of 240 Ry in real space was basically used for the numerical integration and for the solution of the Poisson equation [20]. For bulk systems, cell vectors and internal coordinates are simultaneously optimized without any constraint by using a combination scheme of the rational function (RF) method [21] and the direct inversion iterative sub-space (DIIS) method [22] with a BFGS update [23–26] for the approximate Hessian. For material surfaces (slab models), only internal coordinates are optimized under fixed lattice and a few fixed bottom layers. The force on each atom was relaxed to be less than 0.0003 Hartree/Bohr.

Calculations of the local RCPs and the kinetic energy density were performed by FLPQ module [12] in QEDalpha package [27]. FLPQViewer [13] and Speck [28] were used for visualization of the atomic structures, RCPs, and other properties. Similar functions are available in 3D Viewers such as OpenMX Viewer [29] and Fermisurfer [30]. The atomic unit is used for $\mu_R^\tau(\vec{r})$ (i.e. 1 Hartree/Bohr^3 = 183.631 eV/Å^3).

Computational data are available at the ISSP data repository [31–33].

References

[1] C.-C. Lee, Y. Yamada-Takamura, and T. Ozaki, J. Phys. Condens. Matter **25**, 345501 (2013).

[2] T. Ozaki and C.-C. Lee, Phys. Rev. Lett. **118**, 026401 (2017).

[3] Y. Adachi, R. Zhang, X. Wang, M. Fukuda, T. Ozaki, and Y. Sugimoto, Applied Surface Science **630**, 157336 (2023).

[4] R. Zhang, Y. Yasui, M. Fukuda, T. Ozaki, M. Ogura, T. Makino, D. Takeuchi, and Y. Sugimoto, Nano Letters **25**, 1101 (2025).

[5] R. Zhang, Y. Yasui, M. Fukuda, M. Ogura, T. Makino, D. Takeuchi, T. Ozaki, and Y. Sugimoto, Phys. Rev. Res. **7**, 023036 (2025).

[6] T. Ozaki et al., OpenMX *package*, `http://www.openmx-square.org/`.

[7] M. Fukuda, M. Senami, Y. Sugimoto, and T. Ozaki, arXiv preprint arXiv:2505.04053 (2025).

[8] A. Togo and I. Tanaka, arXiv preprint arXiv:1808.01590 (2018).

[9] P. Pou, S. A. Ghasemi, P. Jelínek, T. Lenosky, S. Goedecker, and R. Pérez, Nanotechnology **20**, 264015 (2009).

[10] S. Jarvis, A. Sweetman, J. Bamidele, L. Kantorovich, and P. Moriarty, Phys. Rev. B **85**, 235305 (2012).

[11] Y. Sugimoto, A. Yurtsever, M. Abe, S. Morita, M. Ondráček, P. Pou, R. Pérez, and P. Jelínek, ACS Nano **7**, PMID: 23906095, 7370 (2013).

[12] M. Fukuda, FLPQ *package*, `https://github.com/mfukudaQED/FLPQ`.

[13] M. Fukuda, FLPQViewer, `https://github.com/mfukudaQED/FLPQViewer`.

[14] W. Kohn and L. J. Sham, Phys. Rev. **140**, A1133 (1965).

[15] J. P. Perdew, K. Burke, and M. Ernzerhof, Phys. Rev. Lett. **77**, 3865 (1996).

[16] I. Morrison, D. M. Bylander, and L. Kleinman, Phys. Rev. B **47**, 6728 (1993).

[17] T. Ozaki, Phys. Rev. B **67**, 155108 (2003).

[18] T. Ozaki, *Standard basis sets of openmx*, Available at `https://www.openmx-square.org/openmx_man3.9/node27.html`.

[19] K. Lejaeghere, G. Bihlmayer, T. Björkman, P. Blaha, S. Blügel, V. Blum, D. Caliste, I. E. Castelli, S. J. Clark, A. Dal Corso, S. de Gironcoli, T. Deutsch, J. K. Dewhurst, I. Di Marco, C. Draxl, M. Dułak, O. Eriksson, J. A. Flores-Livas, K. F. Garrity, L. Genovese, P. Giannozzi, M. Giantomassi, S. Goedecker, X. Gonze, O. Grånäs, E. K. U. Gross, A. Gulans, F. Gygi, D. R. Hamann, P. J. Hasnip, N. A. W. Holzwarth, D. Iuşan, D. B. Jochym, F. Jollet, D. Jones, G. Kresse, K. Koepernik, E. Küçükbenli, Y. O. Kvashnin, I. L. M. Locht, S. Lubeck, M. Marsman, N. Marzari, U. Nitzsche, L. Nordström, T. Ozaki, L. Paulatto, C. J. Pickard, W. Poelmans, M. I. J. Probert, K. Refson, M. Richter, G.-M. Rignanese, S. Saha, M. Scheffler, M. Schlipf, K. Schwarz, S. Sharma, F. Tavazza, P. Thunström, A. Tkatchenko, M. Torrent, D. Vanderbilt, M. J. van Setten, V. Van Speybroeck, J. M. Wills, J. R. Yates, G.-X. Zhang, and S. Cottenier, Science **351**, aad3000 (2016).

[20] T. Ozaki and H. Kino, Phys. Rev. B **72**, 045121 (2005).

[21] A. Banerjee, N. Adams, J. Simons, and R. Shepard, The Journal of Physical Chemistry **89**, 52 (1985).

[22] P. Csaszar and P. Pulay, Journal of Molecular Structure **114**, 31 (1984).

[23] C. G. BROYDEN, IMA Journal of Applied Mathematics **6**, 76 (1970).

[24] R. Fletcher, The Computer Journal **13**, 317 (1970).

[25] D. Goldfarb, Mathematics of Computation **24**, 23 (1970).

[26] D. F. Shanno, Mathematics of Computation **24**, 647 (1970).

[27] M. Senami, K. Ichikawa, A. Tachibana, M. Fukuda, and K. Soga, QEDalpha *package*, `https://github.com/mfukudaQED/QEDalpha`.

[28] R. Terrell, Speck, `https://github.com/wwwtyro/speck`.

[29] Y.-T. Lee and T. Ozaki, Journal of Molecular Graphics and Modelling **89**, 192 (2019).

[30] M. Kawamura, Computer Physics Communications **239**, 197 (2019).

[31] M. Fukuda, *Computational data for applied surface science, 157336 (2023).* `https://isspns-gitlab.issp.u-tokyo.ac.jp/masahiro.fukuda/T4_silicene_Si_adatom_on_Ag111`, 2023.

[32] M. Fukuda, *Computational data for nano letters* **25***, 1101 (2025).* `https://isspns-gitlab.issp.u-tokyo.ac.jp/masahiro.fukuda/C001_dimer_chain_AFM`, 2025.

[33] M. Fukuda, *Computational data for phys. rev. research* **7***, 023036 (2025).* `https://isspns-gitlab.issp.u-tokyo.ac.jp/masahiro.fukuda/C001_dimer_ribbon_AFM`, 2025.